Article:
Fu, Z., Fan, C. orcid.org/0000-0001-5684-2547, Liu, Y. orcid.org/0000-0002-9367-3532 et al. (5 more authors) (2026) Insights into the oxidation regime of diesel soot during realistic DPF regeneration. Fuel, 403. 136086. ISSN 0016-2361

https://doi.org/10.1016/j.fuel.2025.136086

Insights into the oxidation regime of diesel soot during realistic DPF regeneration

Zheng Fu[a,b], Chenyang Fan[a*], Ye Liu[c], Ze Guan[a], Mingliang Wei[a], Bin Xu[a], Tansu Shang[b], Weiwei Shang[a]**

[a] *Henan Provincial International Joint Laboratory of Energy Conservation and Pollutant Control of Energy Power Equipment, College of Vehicle and Traffic Engineering, Henan University of Science and Technology, Luoyang 471003, China*

[b] *State Key Laboratory of Intelligent Agricultural Power Equipment, Luoyang 471003, China*

[c] *Institute for Transport Studies, University of Leeds, Leeds LS2 9JT, UK*

Corresponding author 1. Chenyang Fan

E-mail address: *fanchenyang@haust.edu.cn; fanchenyang@tju.edu.cn*

Postal address: *Vehicle & Transportation Engineering Institute, Henan University of Science and Technology, Luoyang 471003, China*

****Corresponding author 2. Ye Liu***

E-mail address: *Y.Liu8@leeds.ac.uk*

Postal address: *Institute for Transport Studies, University of Leeds, Leeds LS2 9JT, UK*

Abstract

Optimal DPF regeneration methodologies need detailed knowledge of soot oxidation regime under realistic engine conditions. This work experimentally explored the soot oxidation regime during DPF regeneration at inlet temperatures of 300℃ and 350℃. A high-resolution transmission electron microscope (HRTEM) and a Raman spectroscopy were used to observe the structure evolution and explain the oxidation regime transformation during regeneration. Results showed that at the DPF-inlet temperature of 300℃, partial soot particles possessed localized hollow interiors with thicker boundaries at the later stage of its oxidation process, indicating the occurrence of internal burning. However, at the DPF-inlet temperature of 350℃, soot particles exhibit no voids and became more ordered over the whole soot oxidation process, which agree well with the behavior induced by surface oxidation. At the early regeneration stage under at 300 ℃ DPF inlet temperature, soot oxidation led to the extension of micropores, increasing the accessibility of oxygen penetration to particle core. Reversely, the oxidation at higher temperature of 350℃ and the late oxidation stage of 300 ℃ consumed the micropores and shrank the primary particle size, accompanying with the

oxidation-induced graphitization. Oxidation-induced disordering was interesting observed at the early stage of 300 ℃ regeneration, with the ever shorter fringe, larger tortuosity and separation distance, and rising peak area ratio of D1 to G band. Evolutions of structure and defect sites revealed the inclination of internal burning at lower DPF regeneration temperatures, and the prevalence of surface oxidation during the overall process of higher temperatures.

Key words: Soot oxidation; DPF regeneration; Soot structure; HRTEM; Raman spectroscopy

1. INTRODUCTION

Diesel Particulate Filters (DPF) are becoming mandatory for many Heavy-Duty Vehicles (HDV) and Non-Road Mobile Machinery (NRMM) applications to meet the latest major emission regulations[1, 2]. Herein, Channel structured honeycomb based particulate filters were widely used for filtration of PM from diesel engine emissions by trapping particulate matter in their porous walls as exhaust flows through alternate plugged channels, offering high filtration efficiency with manageable backpressure [3, 4]. During the filtration of DPF, the consecutive accumulation of PM on the porous filter walls and inner pore surfaces induces increased pressure drop, resulting in deterioration of the fuel economy and PM emissions if the filters are not cleaned regularly [5-8]. Thus, to ensure the filtration efficiency of DPF, it is essential to conduct regular DPF regeneration by oxidizing the deposited PM that mainly consists of soot particles [9-11].

Motivated by the optimizing of DPF regeneration strategies, the oxidation characteristics of diesel soot under realistic engine and DPF conditions have been investigated in numerous studies [12, 13]. For the non-catalyzed regeneration process,

61 soot particles were oxidized (combusted) at the typical low (<800°C) temperature
62 conditions [14, 15]. In this case, the soot reactivity, defined as the soot tendency to be
63 oxidized at high rate, acts as the primary factor in the rate of filter regeneration. Soot
64 with higher reactivity may lead to faster filter regeneration and slower (or even no)
65 accumulation in the filter. Soot reactivity depends on the surface chemistry and the
66 internal nanostructure [16]. For example, Zheng et al. [17] stated that the ammonia
67 addition into the ethylene diffusion flames led to lower oxidative activity of soot
68 particles, which was assigned to the longer fringes and higher graphitization degrees
69 (defined as the C sp^2/sp^3 hybridization ratio on soot surfaces). Wei et al. [18] found a
70 higher soot reactivity for the methanol-diesel bi-fuels with higher methanol content,
71 corresponding to the lower aggregate compactness, smaller primary particle size and
72 more active aliphatic C-H groups in comparison with the soot from pure diesel fuel. Guo
73 et al. [19] found that biodiesel-generated soot was more reactive with more mass loss at
74 lower temperature range and requires lower temperatures to reach the critical point for
75 DPF regeneration in comparison with the particles from diesel fuels. Their chemical
76 structure studies showed that the fuel blended with oxygenated biofuels generated more

77 active sites and less sp^2 bonds relative to the diesel fuel. The correlation of the oxidation
78 process and soot chemical structure gave insight that soot structure was the underlying
79 reason determining the soot oxidation.

80 The above-mentioned studies support that the disordered structure may provide
81 more number and accessibility of potential reactive edge site of carbon layers within the
82 soot particles. Additionally, further insight into the correlation between soot oxidation
83 and structure demonstrates that the soot structure may also determine the oxygen
84 diffusion, both external, to reach the soot surface, and internal, inside the carbon layers.
85 As stated in the study of Song et al. [20], diesel soot derived from neat biodiesel (B100)
86 underwent a unique oxidation process during the isothermal process of 500°C in air:
87 from initial to 40% oxidation degree, the oxidation behavior induced removal of the
88 amorphous aliphatic carbon-rich sections on the soot surfaces, coinciding with the
89 reduction in the diameter of primary particles, which was considered as the surface
90 burning dominance period; from 40% to 70% oxidation degree, the individual primary
91 particles transformed to a typical structure with hollow inside and long-and-straight
92 outer graphene layers. This structure was assigned to the occurrence of two factors (i.e.,

93 the initial oxygen groups to remove the outermost ordered shell of the particle and the
94 accompanying micropore development for inner core removal). This process was a
95 typical internal burning stage and possessed the fastest rate of oxidation in the whole
96 oxidation process. After the internal burning, the increase in layer mobility led to layer
97 rearrangement and coalescence where the wavy layers become much flatter and longer.
98 The transformation of oxidation mode was also found by Seong et al. [21] during the
99 isothermal oxidation of soot from GDI engine and the substituted Printex-U (PU), with
100 8% O_2 conditions in the TGA tests. They reported that about 50~70% and almost all
101 the primary particles were internally burned for the 67% oxidized soots and 90%
102 oxidized soots, respectively. In contrast, no voids were observed at the early stage of
103 soot oxidation (33% burnoff).

104 Previous studies reveal the high affinity of soot structure with the soot oxidation
105 regime that exerts significant influence on the oxidation rates, at the low-temperature
106 conditions of TGA tests in representative of the DPF regeneration process. However, the
107 previous studies focused on the oxidation of soot samples taken from engine exhaust.
108 The soot oxidation under real DPF regeneration process has not been well investigated.

As suggested in the studies of [20, 22], the internal burning of soot particles can result in an increase in surface area of the particles as combustion proceeds. However, the surface oxidation of soot particles shrinks the particle size and can only consume the carbon atoms on the periphery of particles. Therefore, at the given oxidation conditions, the occurrence of internal burning corresponds to a higher reaction rate than that for the surface burning. In this case, the determination of soot oxidation regime is conducive to establishing a more accurate prediction model for the soot oxidation rate and DPF regeneration behavior. Furthermore, the different soot oxidation regimes can also result in distinct emission characteristics, structural features and chemistry of soot particles. For instance, the soot breakup caused by internal oxidation can lead to an increase in the number of small-sized particles, thus affecting the number and size distribution of particles [3]. In addition, different oxidation regimes may exert distinct impacts on the surface structure and chemical properties of soot that are important factors influencing the further oxidation of soot. Therefore, studying the soot oxidation regimes can more accurately reveal the oxidation mechanism of soot. In this case, the current work was conducted to examine the soot nanostructures, their effects on oxidation regime during

125 real DPF regeneration period, and finally efficacy on the DPF regeneration behavior.
126 Soot samples were derived from the DPF channels under various times during the
127 regeneration period. After that, the development of micro-pores, morphology,
128 nanostructure, size of primary particles, and size and defects in the basal plane of
129 individual graphene layers within the soot particles were further analyzed by
130 Transmission Electron Microscope (TEM) and Raman spectroscopy, respectively, to
131 better understand oxidation regime during real DPF regeneration process.

132 **2. EXPERIMENTAL**

133 *2.1 Sample preparation*

134 Soot samples used in this study were collected from a noncatalyzed cordierite DPF
135 connected to the exhaust pipe of a 4.33L, turbo-charged, 4-cylinder non-road machinery
136 diesel engine. Before DPF regeneration, the engine was operated at 1500 rpm, 123Nm
137 for soot loading. After that, the engine was switched to the high-temperature exhaust
138 conditions of 2200 rpm with 175 Nm (54.84% of the maximum load) and 251 Nm (78.66%
139 of the maximum load) to initiate the DPF regeneration and to achieve the inlet DPF
140 temperatures of 300 and 350 ℃, respectively. The exhaust gas composition (NO, NO_2

and O_2, the potential oxidant for soot oxidation at regeneration-like conditions) at the inlet of DPF system at the DPF regeneration condition is shown in Fig. 1. The minimum and maximum levels of backpressures at downstream of DPF were monitored by the pressure transducer to determine when the DPF regeneration initiated and terminated, respectively. The particle sampling was repeated at various times after the start of DPF regeneration to trace the evolution of particle properties during the regeneration process.

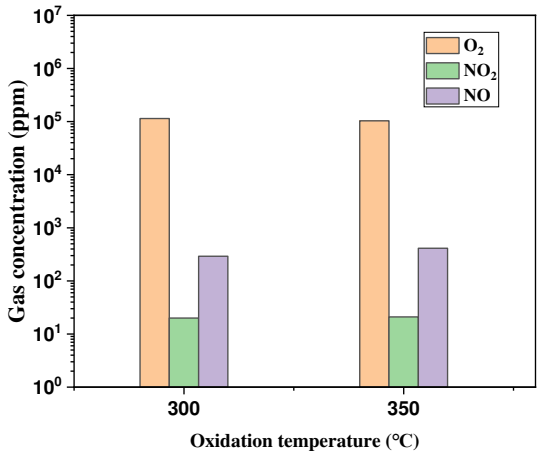

Fig. 1 Composition of exhaust gas at the DPF inlet under the DPF regeneration condition

The raw particle emissions were sampled from the centerline section inside the DPF according to the method used in our previous studies [18, 23]. To obtain the samples used for TEM tests, the particles inertially collided onto the TEM grid inserted to the sampling pipe. The soot-laded TEM grids were further scoured using alcohol to

154 minimize the effects of soluble fractions on TEM tests. For Raman analyses, the particle
155 samples were collected to Teflon filters (R2PJ047，Pall) with the assistance of a vacuum
156 pump at 0.12 L/min gas flow rate. The duration time for particle sampling was adjusted
157 depending on the sample amount. After sampling, the filters were further acoustically
158 treated in ethanol to separate the soot from filters and remove the soluble fractions. After
159 arefaction, the resulting soot samples without soluble impurities were sealed in drying
160 cans for further analysis.

161 *2.2 Sample characterization*

162 A high-resolution transmission electron microscope (HRTEM, Talos F200x, FEI)
163 was applied to assess the morphological and nano-structural information of soot
164 particles. The procedures of digitization and lattice fringe analysis of the TEM images
165 are available in the literatures of [24-26]. Because of the heterogeneous nature of diesel
166 combustion and the concurrent of soot formation and oxidation processes, the soot
167 particles sampled from DPF tunnels may contain a mixture of young and mature soot at
168 various stages of growth and oxidation. Especially for the HRTEM analysis, the
169 HRTEM images may show different structure of the soot samples despite of the same

condition. Fortunately, abundant HRTEM images of these soot samples can be analyzed at each condition to provide the statistical structural information of these soot particles (i.e. the typical properties of the majority of soot particles). In the present work, more than 100 particles were randomly selected from different aggregates in the HRTEM images for each soot sample to eliminate subjective influences and minimize the test uncertainty. With the random statistical method, the test uncertainty of the parameters derived from HRTEM images is no more than 5%.

According to NLDFT (Non Local Density Functional Theory) approach, the micropores on soot surfaces are supposed to be located between the BSU (commonly described as stacks composed of 2~4 parallel planar graphene sheets) and even between the parallel aromatic sheets constitutive of a BSU. The average micropore width in the range of up to 2 mm was directly deduced from pore size distribution (PSD) derived by the NLDFT revisited by Pré et al. [27]. Combined with the 2-disk finite pore model [28], the ratio of the disk diameter over the distance separating the parallel walls was imposed to be 6, and finally used to calculate the surface area of micropores. In addition, when calculating the surface area of the particle, only the surface of the spherical primary

186 particles was assumed to be accessible for oxidation reactions. Therefore, the surface
187 area of particle equals to that for the sphere with the diameter of primary particle size
188 derived from TEM analysis.

189 Size and defects in the basal plane of individual graphene layers within the soot
190 particles (graphitization degree) of soot particle was determined by a Raman scattering
191 spectrometer (DXR, Thermo Scientific). The excitation laser was a He-Ne ion laser with
192 a wavelength of 532 nm and source power of 20 mW. The laser was focused onto the
193 sample using a microscope objective lens (50×). During each measurement, the Raman
194 spectra were recorded at approximately 10 positions to reduce the measure uncertainty
195 arouse from the sample inhomogeneity to <5%, with an acquisition time of 60 s and a
196 hardware accumulation of 3 times to reduce noise in the spectra.

197 **3. Results & discussion**

198 In this study, investigations on soot property and soot oxidation regimes are
199 conducted at the DPF inlet temperatures of 300 ℃ and 350 ℃. One may argue that the
200 soot oxidation by oxygen can only be initiated at the temperature higher than 500 °C.
201 According to the findings of Meng et al. [29], prior to the regeneration stage, DPF

underwent a temperature rise stage where the temperature within DPF substrate increased from ~200°C (at the DPF inlet) to the upper detection limit (1200°C) of the used K-type thermocouple. In fact, on their particulate loading system, most of the regeneration period occurred at the temperature of 475°C to 575°C which is sufficient to ignite the soot particles. In their work, the oxidant for soot oxidation reactions was air offered by an air compressor. However, due to the presence of NO_2 in the realistic exhaust gas, some soot particles can be ignited at 250~450°C [30] during the realistic active regeneration. As an example, the results of Toumasatos et al. [31] revealed that the exhaust temperature measured in front of the DPF inlet was in range of about 180~300 °C during the DPF regeneration period of the typical real drive emission (RDE) compliant tests on a commercially available Euro 6d-temp diesel-powered vehicle. That is, studies on the soot property at the DPF inlet temperature of 300°C and 350°C is rational to understand the soot oxidation regime during the DPF regeneration of the modern diesel-powered vehicles.

3.1 Soot structure

Figures 2 and 3 display the nanostructure of soot particles along with DPF

218 regeneration at the DPF inlet temperatures of 300 ℃ and 350 ℃, respectively. Under
219 the lower temperature (300 ℃), soot particles show localized hollow interiors with
220 thicker boundaries at the later stage of its oxidation process. Correspondingly, at higher
221 DPF inlet temperatures (350 ℃), soot particles evolve to a more ordered structure at
222 either the exterior or the internal sections along with the regeneration process and exhibit
223 no voids within the primary particles.

224 The oxidation-induced graphitization during regeneration may be the primary
225 factor for the increasing ordered structure: during oxidation, the C atoms on the
226 perimeter are gradually consumed with concurrent densification and size reduction,
227 which is called as surface oxidation regime. Regarding to the generation of voids in the
228 interior, there are some controversies: (1) as stated by Hurt et al. [32], the internal
229 oxidation, which can induce internal voids, might take place at the early stage of
230 oxidation, according to the higher total surface area than the external surface area of the
231 primary particles. Moreover, the internal oxidation was considered as the prerequisite
232 for homogeneous reaction-induced densification; (2) Song et al. [20] proposed that the
233 internal burning occurred at the medium stage of oxidation, arising from the penetration
234 of micropores to the particle core and consumption of more reactive internal carbon,
235 finally leading to the hollow-inside structure.

As discussed in the study of Ghiassi et al. [22], soot burning by O_2 depends upon the rate of oxygen diffusion versus surface reaction at the temperature of interest. Gilot et al. [33] and Marcucilli et al. [34] showed that the increase in the surface area induced by the oxygen penetration was greater at 600 °C than at 800 °C. This observation is consistent with significant oxygen penetration at low temperature due to slower consumption by reaction [14]. In addition, the soot surface gradually deactivates along the oxidation process due to the oxidation-induced graphitization and consumption of the active sites. The deactivation leads to a lower reaction rate and allows longer time for oxygen diffusion from particle periphery to the core, and increases the occurrence potential of internal burning. As the method proposed by Ghiassi et al. [22], the time scale for oxygen diffusion is positively correlated with the tortuosity (τ) that is defined as the ratio of the distance of oxygen travels through the slits between crystallites to the radius of primary particles. At the latter regeneration stage, the surface oxidation also leads to shrinking of the primary particle size, and then shortens the pathway of oxygen penetration. Consequently, the internal oxidation is prone to occur at the low-temperature and in the middle and late stages.

In summary, the regime of soot oxidation may be transformed along with the oxidation process, accompanying by the mobility of soot structures in terms of micropore development, lamella size and tortuosity, and size of primary particles. In consequence, these factors are further investigated in the following sections.

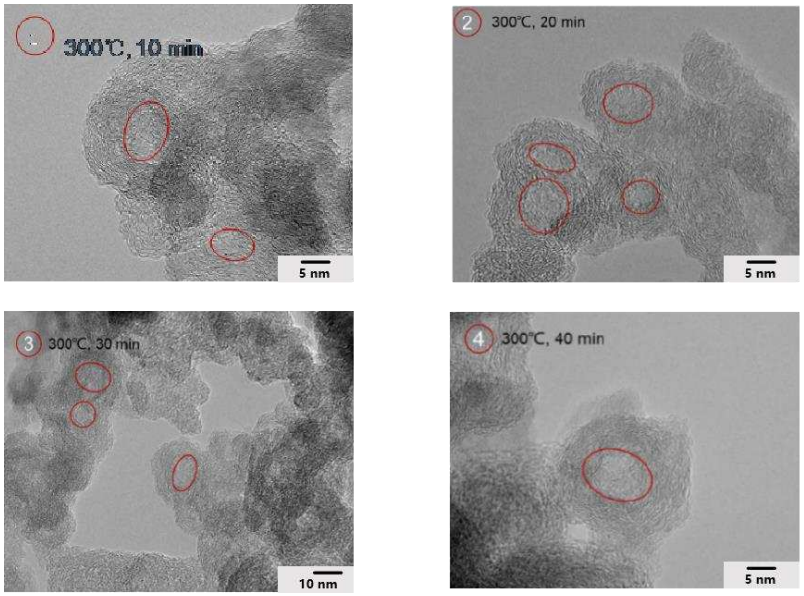

Fig. 2 Evolution of nanostructure of soot particles with oxidation time during 10~40 min at the temperature of 300 ℃

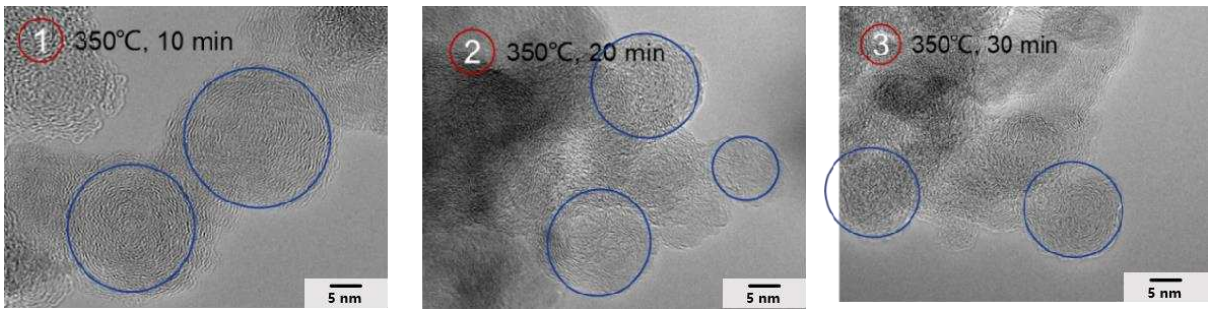

Fig. 3 Changes of nanostructure of soot particles with oxidation time during 10~30 min at the temperature of 350 ℃

3.2 Development of primary particle size and micropore

The size (diameter) of primary particles (d_p) is derived from the TEM images demonstrated in Figs. 4 and 5. As can be seen, the agglomerated particles present chain and cluster-like structures and consist of hundreds of primary particles of different sizes. To get a statistically relevant number of measurements, several freely chosen single particle agglomerates were taken into account for the d_p measurement.

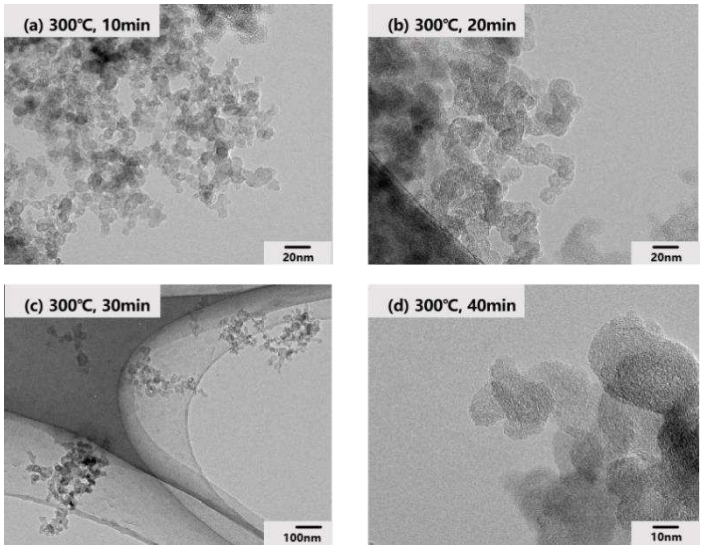

Fig. 4 TEM images for soot particles at various regeneration time under the DPF inlet temperature of 300 ℃

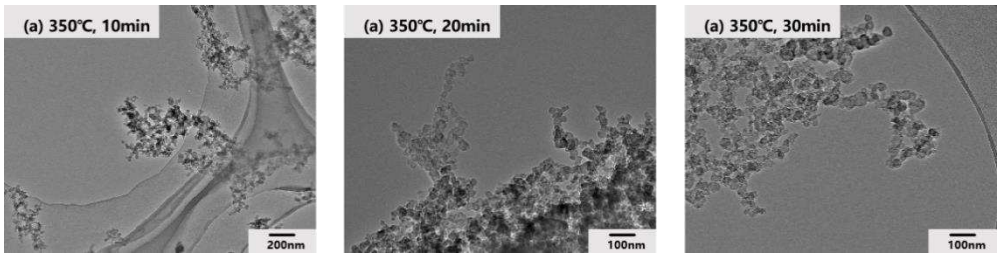

Fig. 5 TEM images for soot particles at various regeneration time under the DPF inlet temperature of 350 ℃

Figures 6 and 7 display the d_p distribution for soot sampled at various stages of the DPF regeneration process at inlet temperatures of 300°C and 350°C, respectively. It is observed that the size distribution of primary particles for each soot sample shows a similar lognormal pattern and exhibits no significant difference on an intuitive observation. Statistically, during the 300 °C DPF regeneration process, when the soots were sampled at 10, 20, 30, and 40 minutes respectively, 50% of the primary particles had sizes smaller than 17 nm, 19 nm, 16.5 nm, and 16.5 nm. Correspondingly, in the

350 °C regeneration process, for the soots collected at 10 minutes, 20 minutes, and 30 minutes, 50% of the primary particles were smaller than 14.5 nm, 15.5 nm, and 12.5 nm respectively. The mean size of primary particles is also calculated by integrating the d_p distribution and shown in Figs. 5 and 6. Under 300 ℃ DPF inlet temperature, the mean d_p shows an increase from 18.01 nm to 19.91 nm as the regeneration undergoes from 10 min to 20 min; after 20 min, the mean d_p exhibits a general reduction and achieves 16.67 nm at 40 min. At the early stage, the shrinking of spherical particles is mild due to the lower rate of surface oxidation, whereas the increase of soot size induced by continuous surface growth is prevalent, finally resulting in the increase in d_p. At the later oxidation stage, the occurrence of internal burning (as depicted in the HRTEM images,) may increase the potential of particle breakup, forming more smaller particles. moreover, the concurrently surface oxidation may also consume the carbon atoms on the periphery and reduce the size of primary particles. Correspondingly, during the regeneration period of 10 min to 30 min, the mean d_p shows a decrease from 17.71 nm to 13.79 nm with proceeding oxidation under 350 ℃ DPF inlet temperature. As depicted by the HRTEM images, the surface oxidation at 350 ℃ condition can be responsible for the general

reduction of mean d_p.

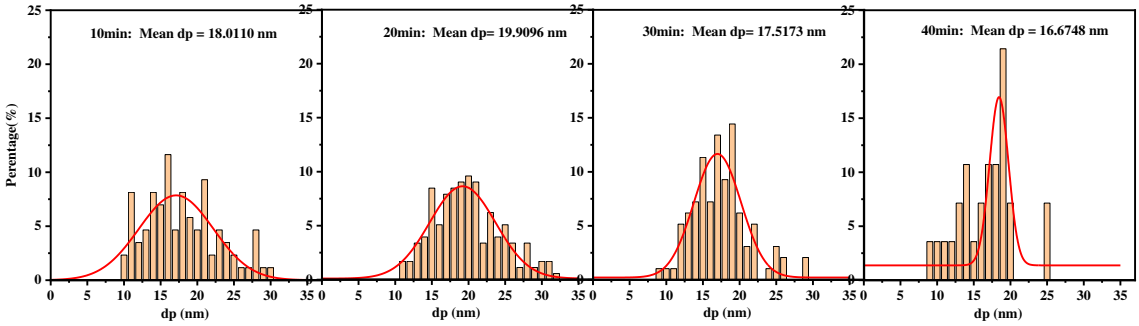

Fig. 6 Distributions of primary particle size at various regeneration time under the DPF inlet temperature of 300 ℃

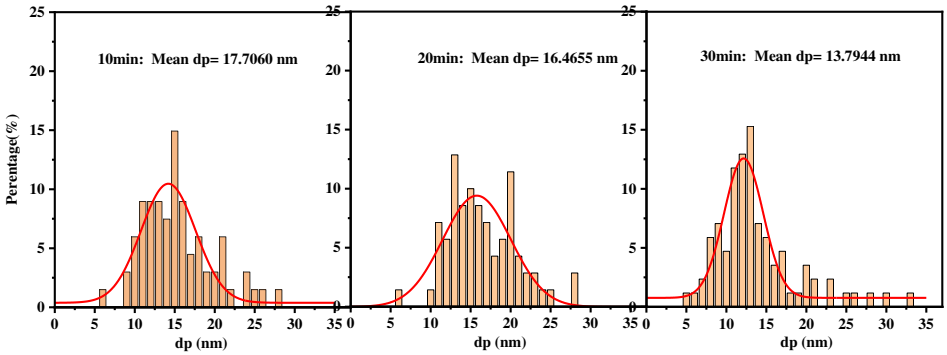

Fig. 7 Distributions of primary particle size at various regeneration time under the DPF inlet temperature of 350 ℃

As proposed by Song et al. [20], micropore penetration is the plausible factor for internal oxidation. In addition, surface micropores can provide additional active surface area for the oxidation reactions without affecting the reactivity of the soot particles. Therefore, the evolution of micropores is also assessed to reveal the oxidation regime. Distributions of pore width on soot surfaces for 300 and 350 ℃ DPF inlet temperature are respectively displayed in Figs. 8 and 9. The pore size exhibits the half-normal

distribution for each soot sample. The distribution is further integrated to obtain the mean size of pores. Under 300℃ DPF inlet temperature, the mean pore size shows a slight decrease at the early stage of 10~20min, and significant increase as the regeneration evolves to the latter stages (30~40min). In contrast, the mean pore size possesses a general reduction along with the regeneration process under 350 ℃ DPF inlet temperature. Pore radii of 2.5 nm and larger are taken to represent unfilled space between the primary particles within an aggregate. For the soot oxidation by O_2, the O_2 molecules are easy to penetrate into the space between the units of aggregates and reach the surface of primary particles, due to the larger porosity of soot aggregates [35]. Therefore, the oxidation reactions for soot particles is on the scale of primary particle size, and can be reduced to oxidation of spherule units[36]. That is, the pores with 0.5~1 nm radii representing the actual micropores in the spherical of primary particles are related to the oxidation regime of soot particles rather than the larger pores between the spherules. Therefore, pores smaller than 1nm in radii are assessed to explain the oxidation regime.

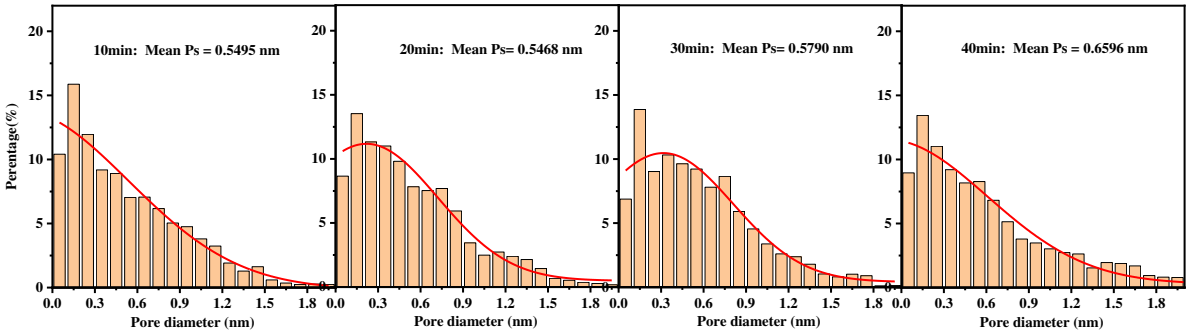

Fig. 8 Distributions of pore size on soot surfaces at various regeneration time under the DPF inlet temperature of 300 ℃

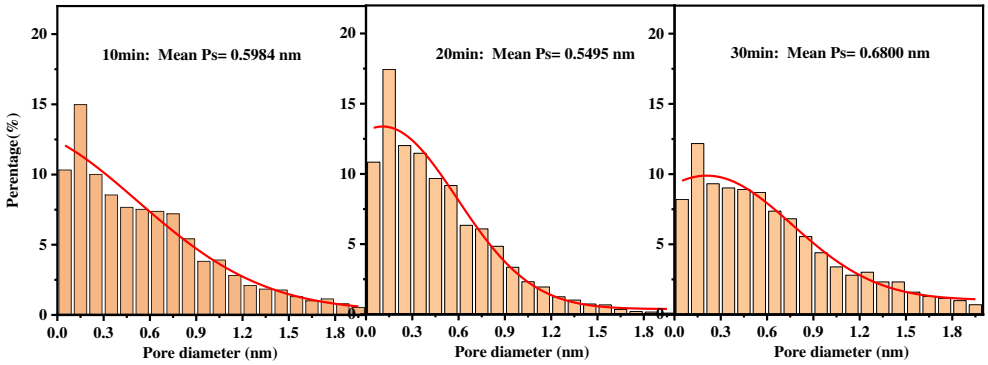

Fig. 9 Distributions of pore size on soot surfaces at various regeneration time under the DPF inlet temperature of 350 ℃

According to Neoh et al [37], the development of surface micropores and the ratio of surface area provided by the micropores (radii≤1 nm) can be used to explain the potential of soot internal burning. Figure 10 shows the ratio of surface area provided by <1 nm pores (A_{pore}) to the area of spherical primary particles (A_{sphere}) under 300 and 350 ℃ DPF inlet temperature. For soot obtained at 300 ℃, the pore area is found to be about 4~6 times the external area of the spheres. Furthermore, soot particles show a reduction in A_{pore}/A_{sphere} at the early stage of 10~20 min and final stage of 30~40min during the

regeneration process. However, a significant increase of A_{pore}/A_{sphere} are observed at the medium stage of 20~30 min. Apart with the surface area accessible on the defects of the units itself, pores can provide additional areas for the oxidation reactions. During the oxidation-induced graphitization, the progressive growth of lamella planes within primary particles reduces the porosity. Moreover, the decrease of A_{pore}/A_{sphere} suggests the prevalence of shrinking in pore to that for the primary particle. The increasing A_{pore}/A_{sphere} at the medium stage of DPF regeneration may be attributed to the pore development and rapid consumption of carbon atoms at the exterior region.

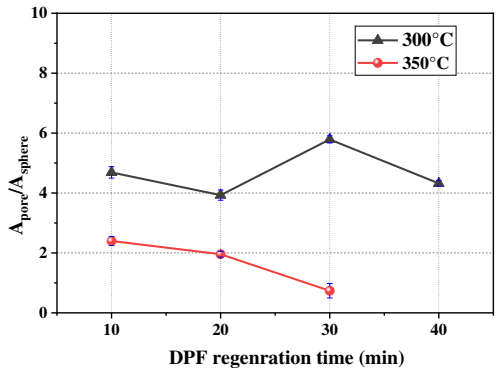

Fig. 10 Ratio of pore surface area to the area of spherical particles for soot from 300 and 350℃ DPF inlet temperature

3.3 Development of lattice fringe

HRTEM images are further studied to examine the nanostructure of primary particles in terms of fringe length (L_a), fringe tortuosity (T_f) and separation distance (D_s). Figures 11 and 12 illustrate the distributions of L_a, T_f and D_s for soot samples obtained

353 under the DPF inlet temperature of 300 and 350 ℃, respectively. Across the regeneration
354 at 350 ℃ inlet temperature, there is a progressive graphitization in structure for the soot
355 samples, as manifested by the reduction of the primary particles with shorter length,
356 higher tortuosity and larger separation (corresponding to a less oxidation degree and
357 higher activity). The oxidation-induced graphitization has been widely reported in
358 previous works of [38] and [39], and attributed to the external surface oxidation (via the
359 so-called shrinking core mode). However, different evolution trend of soot structure
360 during oxidation was found in [40] (via HRTEM) and [41] (via X-ray diffractometer).
361 In [40], n-butanol/n-dodecane mixed soot underwent a progressive decrease in structure
362 across the oxidation series, with the ever shorter lamella and increasing curvature in the
363 lamella. They believed that the soot structure reduction arose from the hybrid of external
364 surface oxidation (via the so-called shrinking core mode) and internal burning (i.e.
365 preferential core burnout). Chang et al [41] observed that the size of microcrystal basal
366 plane and interlayer spacing for coal soot and Printex significantly decreased during
367 oxidation, indicating a unexpected disordering process during oxidation. They approved
368 the statement of De Falco et al. [42] who also observed the disordering of lattice after

carbon atoms removal, and the amorphous component was more easily consumed, inducing a sort of graphitization.

For soot particles derived from 300 ℃ regeneration process, a structure disordering is also observed during the early oxidation stage, as illustrated by the slight decrease in L_a, and increase in T_f and D_s during the regeneration period of 10~20min. The predominant of internal burning that admits the oxygen penetration within outer portion of the primary particles and causing breakup of the initial graphene segments may be the plausible factor for the structure disordering [40, 43]. During the regeneration at 20~40min, an ever more ordered structure is observed during the oxidation process, according to the generally increasing L_a and decreasing T_f and D_s. The more ordered soot structure during oxidation suggests the prevalence of surface burning of soot particles.

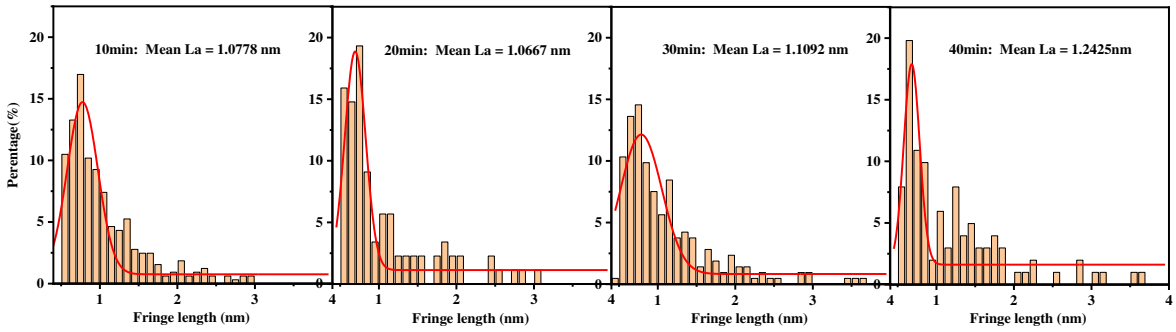

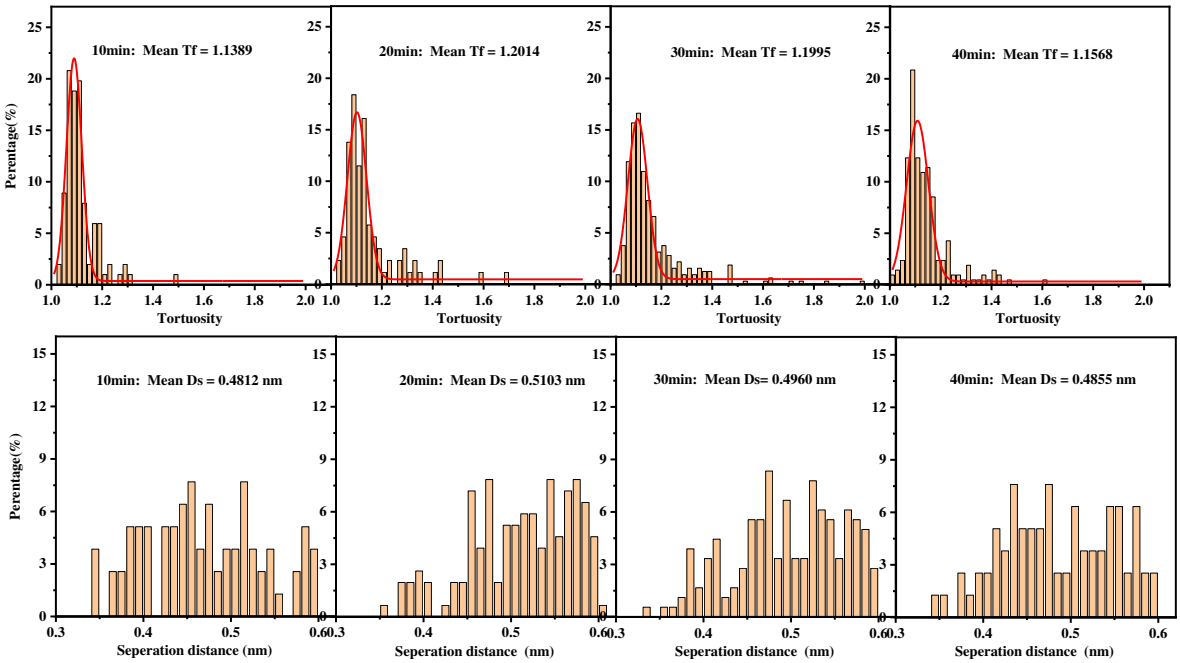

Fig. 11 Fringe length (La), tortuosity (Tf) and separation distance (Ds) for soot from 300℃ DPF inlet temperature

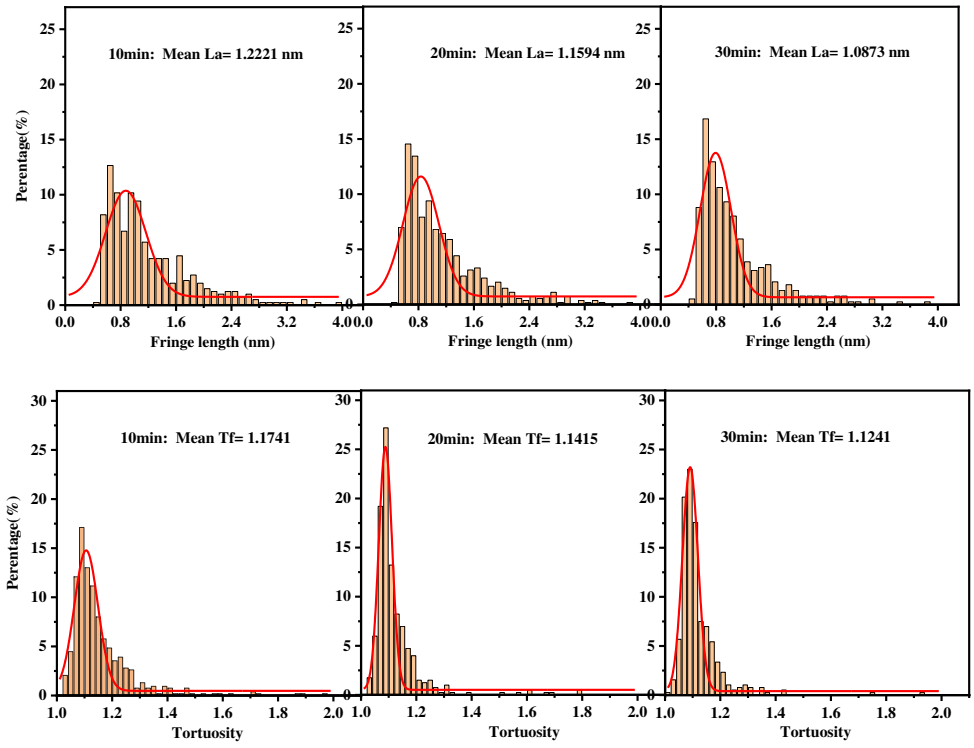

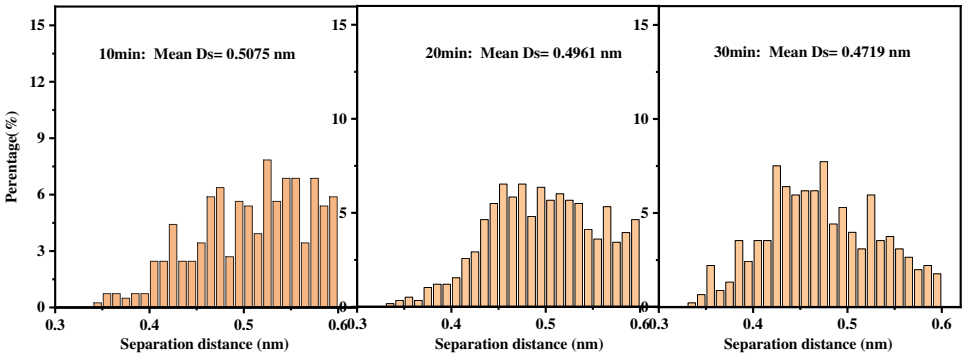

Fig. 12 Fringe length (La), tortuosity (Tf) and separation distance (Ds) for soot from 350℃ DPF inlet temperature

3.4 Defects on soot surfaces

Raman spectroscopy is employed to further reveal the structural evolution along with the DPF regeneration. Fig. 13 displays the Raman spectra for soot samples and the fitting peaks of D1, D3, D4 and G according to the peak assignments of [44-46]. In these studies, the D1 band originates from the carbon atoms located at the edges of the graphene layers. The D4 band is attributed to the C–C and C=C bonds within polyene-like structures, and the G band stems from the ideal graphitic lattice. Meanwhile, the D3 band is assigned to the amorphous carbon fraction present in the soot particles. The above-mentioned band influence the reactivity of the carbon atoms. For instance, the carbon atoms located at the edge of the graphene layers are known to be significantly more reactive than the carbon atoms located at the basal plane [38]. Therefore, there has been many efforts to correlated the overall oxidative reactivity of the soot to the ratio

between the different D bands and the G band intensities and the ratio between their areas [47, 48]. In this work, to quantify the concentration of the defects, the peak area of D1, D3 and D4 is normalized to the G band and termed as A_{D1}/A_G, A_{D3}/A_G and A_{D4}/A_G, respectively. As shown in Fig. 14, under 300 ℃ DPF inlet temperature, soot oxidation during the early DPF regeneration (10~20min) leads to an appreciable increase in A_{D1}/A_G and slight decrease in A_{D4}/A_G, indicating the rises in the edge sites and preferential consumption of the carbon with active amorphous structure. The rising A_{D1}/A_G is coinciding with the afore-mentioned oxidation-induced structure disordering supported by HRTEM tests during 10~20 min regeneration period under 300 ℃ DPF inlet temperature. That is, with oxidation, the breakup of the initial graphene segments gives rise to a greater number of fringes with shorter lengths and an increased amount of carbon atoms positioned at the edge sites [38]. This could be related to the soot oxidation reactivity, since as the edge sites increase, the accessibility for oxygen attack and oxidation reactions is expected to increase. As aforementioned, the occurrence of internal burning depends upon the possibility of oxygen penetration into the particle core before it is consumed by the surface oxidations. The increase in soot reactivity in

418 this stage may shorten the time scale of soot oxidation and permit less accessibility for
419 the oxygen diffusion, thus lessen the internal burning at the early DPF regeneration.
420 During 20~40 min, A_{D1}/A_G and A_{D3}/A_G exhibit a continuous reduction along with the
421 300 ℃ DPF regeneration. These characteristics represent that with the surface oxidation,
422 the carbon atoms on edge sites and with less-ordered structure are gradually oxidized,
423 resulting in the more ordered structure of soot particles (as supported by the HRTEM
424 results). This phenomenon is agreement with that found by Ivleva et al, [49] who
425 followed the structural changes in spark discharge soot and light-duty diesel vehicle soot
426 upon oxidation and gasification by nitrogen oxides and oxygen in a diesel exhaust
427 aftertreatment model system at 250 and 300 ℃. The structure ordering by surface
428 oxidation is also evidenced by the continuous reduction in A_{D1}/A_G and A_{D3}/A_G for soot
429 particles over the whole regeneration process under 350 ℃ DPF inlet temperature.

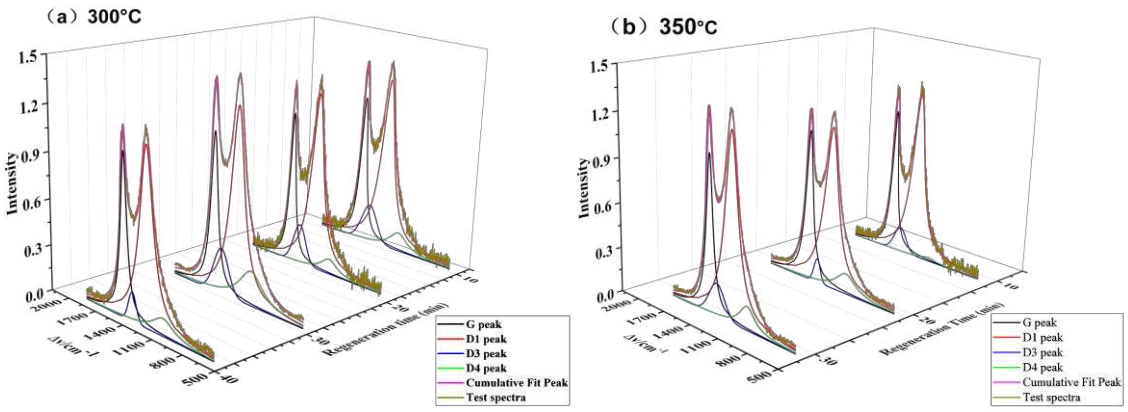

430

431 Fig. 13 Raman spectra and the fitted peaks for soot from 300℃ and 350℃ DPF inlet temperature

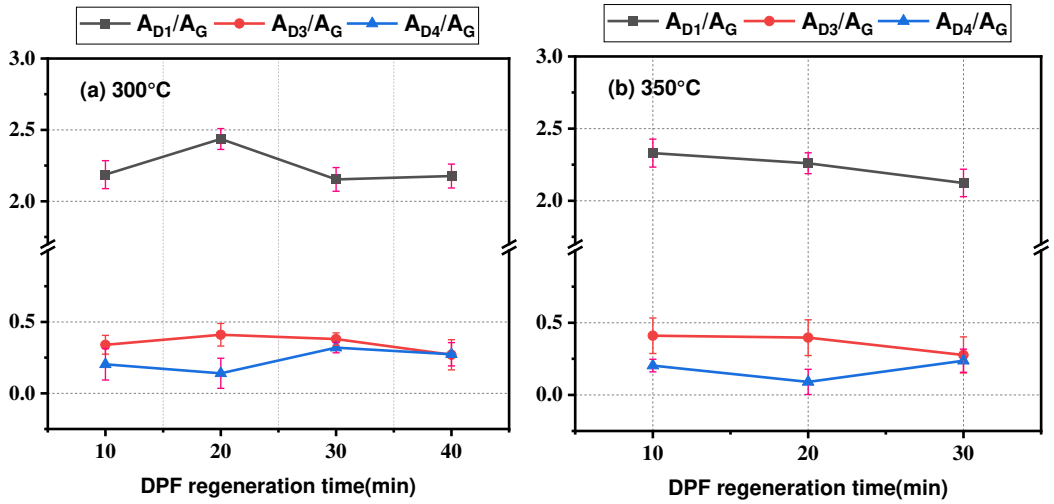

Fig. 14 A_{D1}/A_G, A_{D3}/A_G and A_{D4}/A_G ratios for soot from 300℃ and 350℃ DPF inlet temperature

4. Conclusions

The oxidation regime of soot particles was investigated by studying the structure development during the realistic DPF regeneration process. DPF regeneration was conducted under two typical DPF inlet temperature of 300 and 350℃. From structural analysis, soot particles showed localized hollow interiors with thicker boundaries at the later stage of its oxidation process for 300℃ DPF inlet temperature, representing the occurrence of internal oxidation. Reversely, soot particles derived at the higher temperature of 350℃ exhibit no voids and became more ordered during regeneration, which agree well with the behavior induced by surface oxidation. The oxidation during DPF regeneration at 300 ℃ inlet temperature led to growth of micropores and primary

444 particle size at the early regeneration stage. However, the oxidation at higher
445 temperature of 350℃ and the late oxidation stage of 300 ℃ consumed the micropores
446 and shrank the primary particle size, accompanying with the oxidation-induced
447 graphitization. However, results from HRTEM and Raman spectroscopy evidenced that
448 oxidation-induced disordering was interesting observed at the early stage of 300 ℃
449 regeneration. Structure evolutions revealed the inclination of internal burning at lower
450 DPF regeneration temperatures, and the prevalence of surface oxidation during the
451 overall process of higher temperatures. Internal burning of soot has a tendency to
452 substantially enhance the specific surface area available for soot oxidation.
453 Consequently, augmenting the proportion of particles with the potential for internal
454 combustion presents a viable approach to expedite DPF regeneration in the later stages.
455 Nevertheless, internal combustion can also induce particle fragmentation, leading to an
456 increase in particle counts. Given that modern emission regulations impose constraints
457 on both particle mass and number simultaneously, the influence of the soot oxidation
458 regime on DPF regeneration warrants further in-depth investigation.

459 **5. CRediT authorship contribution statement**

Zheng Fu: Conceptualization, Investigation, Data visualization, Writing-original draft. **Chenyang Fan:** Investigation, Methodology, Funding acquisition, Project administration, Writing-review & editing. **Ye Liu:** Investigation, Methodology, Data visualization. **Ze Guan**: Investigation, Data visualization. **Mingliang Wei**: Investigation, Data visualization. **Bin Xu:** Project administration, Investigation. **Tansu Shang:** Data visualization, Validation. **Weiwei Shang**: Data Curation, Data visualization.

6. Acknowledgments

This research is sponsored by National Natural Science Foundation of China (No. 52006054), and International scientific and technological cooperation project in Henan Province (No. 232102521019)

References

1. Tan, P.-q., et al., *Characteristics of ash formed by different lubricant additives and its effect on DPF performance.* Fuel, 2024. **358**: p. 130287.
2. Cavallo, D.M., et al., *Experimental study on the effect of loading and regeneration for an optimized management of the DPF.* Results in Engineering, 2023. **18**: p. 101048.
3. Huang, J., et al., *A Review of the Application of Soot Catalysts: Focus on the Soot Oxidation-Induced Fragmentation Process.* Energy & Fuels, 2024. **38**(21): p. 20057-20083.
4. Gao, J., et al., *The effect of deposit morphology on soot oxidation in non-catalytic and catalytic processes.* Journal of the Energy Institute, 2024. **116**.
5. Ovaska, T., et al., *Effect of late diesel injection on close-coupled SCR + ASC during DPF regeneration period.* Fuel, 2025. **381**: p. 133406.
6. Li, X., et al., *Study on regenerative exothermic process in ash containing DPF structure based on lattice Boltzmann method.* Case Studies in Thermal Engineering, 2024. **55**: p. 104105.
7. Tan, P., et al., *Pressure drop model of DPF considering ash factor at different capture stages.* Energy, 2023. **283**: p. 128439.
8. Huang, J., et al., *Insight into the penalty of exhaust emissions and fuel consumption by DPF regeneration of a diesel passenger car.* Chemosphere, 2022. **309**: p. 136629.
9. Shi, Y., et al., *Effect of temperature control conditions on DPF regeneration by nonthermal plasma.* Chemosphere, 2022. **302**: p. 134787.
10. Yamamoto, K., H. Kato, and D. Suzuki, *Pressure Response during Filtration and Oxidation in Diesel Particulate Filter.* Emission Control Science and Technology, 2019. **5**(1): p. 24-30.
11. Luo, Y., et al., *Study on the Evolution of Physicochemical Properties of Carbon Black at Different Regeneration Stages of Diesel Particulate Filters Regenerated by Non-Thermal Plasma.* Processes, 2024. **12**(6).
12. Huang, J., et al., *Investigation of the physicochemical properties of soot subjected to non-catalytic and CeO2-catalytic aging under sequential aerobic and anaerobic exhaust-like conditions simulating the transition from engine operation to cessation.* Fuel, 2024. **362**(000): p. 16.
13. Meng, Z., et al., *Comparison of the use of real diesel soot and soot surrogate in the performance analysis of diesel particulate filters.* Journal of Cleaner Production, 2024. **442**(000): p. 17.
14. Stanmore, B.R., J.F. Brilhac, and P. Gilot, *The oxidation of soot: a review of experiments, mechanisms and models.* Carbon, 2001. **39**(2247-2268): p. 2247-2268.
15. Chen, X., et al., *Effect of non-thermal plasma injection flow rate on diesel particulate filter regeneration at room temperature.* Carbon Letters, 2024. **34**(3): p. 1075-1089.
16. Chu, H.Q., et al., *Effects of adding cyclohexane, n-hexane, ethanol, and 2,5-dimethylfuran to fuel on soot formation in laminar coflow n-heptane/iso-octane diffusion flame.* Combustion and Flame, 2021. **225**: p. 120-135.
17. Zheng, J., L. Hu, and S.H. Chung, *Effect of ammonia addition on nanostructure of soot in laminar coflow diffusion flames of ethylene diluted with nitrogen.* Proceedings of the Combustion Institute, 2024. **40**(1): p. 105392.
18. Wei, J., et al., *Impact of methanol alternative fuel on oxidation reactivity of soot emissions from a modern CI engine.* Fuel, 2020. **268**.
19. Guo, Y., et al., *The correlation between diesel soot chemical structure and reactivity.* Carbon, 2020. **161**: p. 736-749.
20. Song, J., et al., *Examination of the oxidation behavior of biodiesel soot.* Combustion and Flame, 2006. **146**(4): p. 589-604.
21. Seong, H. and S. Choi, *Oxidation-derived maturing process of soot, dependent on O2–NO2 mixtures and temperatures.* Carbon, 2015. **93**: p. 1068-1076.
22. Ghiassi, H., et al., *Soot oxidation-induced fragmentation: Part 1: The relationship between soot nanostructure and oxidation-induced fragmentation.* Combustion and Flame, 2015. **000**: p. 1-9.
23. Fan, C., et al., *An assessment of soot chemical property from a modern diesel engine fueled with dimethyl carbonate-diesel blends.* Fuel, 2022. **309**: p. 122220.

24. Toth, P., et al., *A novel framework for the quantitative analysis of high resolution transmission electron micrographs of soot I. Improved measurement of interlayer spacing.* Combustion and Flame, 2013. **160**(5): p. 909-919.
25. Toth, P., et al., *Quantitative differentiation of poorly ordered soot nanostructures: A semi-empirical approach.* Fuel, 2012. **99**: p. 1-8.
26. Toth, P., *Nanostructure quantification of turbostratic carbon by HRTEM image analysis: State of the art, biases, sensitivity and best practices.* Carbon, 2021. **178**: p. 688-707.
27. Pré, P., et al., *A new approach to characterize the nanostructure of activated carbons from mathematical morphology applied to high resolution transmission electron microscopy images.* Carbon, 2013. **52**: p. 239-258.
28. Jagiello, J. and J.P. Olivier, *A Simple Two-Dimensional NLDFT Model of Gas Adsorption in Finite Carbon Pores. Application to Pore Structure Analysis.* Journal of Physical Chemistry C, 2016. **113**(45): p. 19382-19385.
29. Meng, Z., et al., *Study of gas and particulate emission characteristics during the fast regeneration period of DPF.* Fuel, 2022. **317**: p. 123353.
30. Soltani, S., R. Andersson, and B. Andersson, *The effect of exhaust gas composition on the kinetics of soot oxidation and diesel particulate filter regeneration.* Fuel, 2018. **220**: p. 453-463.
31. Toumasatos, Z., et al., *The role of the driving dynamics beyond RDE limits and DPF regeneration events on pollutant emissions of a Euro 6d-temp passenger vehicle.* Journal of Aerosol Science, 2022. **161**: p. 105947.
32. LONGWELL, R.H.H.A.F.S.a.J.P., *Gasification-Induced Densification of Carbons: From Soot to Form Coke.* COMBUSTION AND FLAME 1993. **95**: p. 430-432.
33. Gilot, P., et al., *Determination of kinetic data for soot oxidation. Modeling of competition between oxygen diffusion and reaction during thermogravimetric analysis.* Combustion and Flame, 1993. **95**(1): p. 87-100.
34. Marcuccilli, F., et al., *Experimental and theoretical study of diesel soot reactivity.* Symposium (International) on Combustion, 1994. **25**(1): p. 619-626.
35. Song, J., C.-H. Jeon, and A.L. Boehman, *Impacts of Oxygen Diffusion on the Combustion Rate of In-Bed Soot Particles.* Energy & Fuels, 2010. **24**(4): p. 2418-2428.
36. Zhdanov, V.P., P.-A. Carlsson, and B. Kasemo, *Kinetics of oxidation of nm-sized soot spherules.* Chemical Physics Letters, 2008. **454**(4-6): p. 341-344.
37. Neoh, K.G., J.B. Howard, and A.F. Sarofim, *Effect of oxidation on the physical structure of soot*, in *Symposium (International) on Combustion*. 1985. p. 951-957.
38. Vander Wal, R.L. and A.J. Tomasek, *Soot oxidation: dependence upon initial nanostructure.* Combustion and Flame, 2003. **134**(1-2): p. 1-9.
39. Knauer, M., et al., *Changes in Structure and Reactivity of Soot during Oxidation and Gasification by Oxygen, Studied by Micro-Raman Spectroscopy and Temperature Programmed Oxidation.* Aerosol Science and Technology, 2009. **43**(1): p. 1-8.
40. Jaramillo, I.C., et al., *Soot oxidation kinetics under pressurized conditions.* Combustion and Flame, 2014. **161**(11): p. 2951-2965.
41. Chang, Q., et al., *The structural evolution and fragmentation of coal-derived soot and carbon black during high-temperature air oxidation.* Combustion and Flame, 2020. **216**: p. 111-125.
42. De Falco, G., et al., *The evolution of soot particles in premixed and diffusion flames by thermophoretic particle densitometry.* Proceedings of the Combustion Institute, 2017. **36**(1): p. 763-770.
43. Kelesidis, G.A., P. Crepaldi, and S.E. Pratsinis, *Oxidation dynamics of soot or carbon black accounting for its core-shell structure and pore network.* Carbon, 2024. **219**: p. 118764.
44. Parent, P., et al., *Nanoscale characterization of aircraft soot: A high-resolution transmission electron microscopy, Raman spectroscopy, X-ray photoelectron and near-edge X-ray absorption spectroscopy study.* Carbon, 2016. **101**: p. 86-100.
45. Pahalagedara, L., et al., *Structure and Oxidation Activity Correlations for Carbon Blacks and Diesel Soot.* Energy & Fuels, 2012. **26**: p. 6757-6764.
46. Lapuerta, M., et al., *Effect of fuel on the soot nanostructure and consequences on*

583 *loading and regeneration of diesel particulate filters.* Combustion and Flame, 2012. **159**(2): p.
584 844-853.
585 47. Rohani, B. and C. Bae, *Effect of exhaust gas recirculation (EGR) and multiple*
586 *injections on diesel soot nano-structure and reactivity.* Applied Thermal Engineering, 2017.
587 **116**: p. 160-169.
588 48. Lapuerta, M., J. Rodríguez–Fernández, and J. Sánchez-Valdepeñas, *Soot reactivity*
589 *analysis and implications on diesel filter regeneration.* Progress in Energy and Combustion
590 Science, 2020. **78**: p. 100833.
591 49. Ivleva, N.P., et al., *Raman Microspectroscopic Analysis of Changes in the Chemical*
592 *Structure and Reactivity of Soot in a Diesel Exhaust Aftertreatment Model System.*
593 Environmental Science & Technology, 2007. **41**(10): p. 3702-3707.
594